1   Title: Hydrodynamic regime drives flow reversals in suction feeding larval fishes during early

2   ontogeny

3   Krishnamoorthy Krishnan[1], Asif Shahriar Nafi[1], Roi Gurka[1], Roi Holzman[2,3]

4

5   1) School of Coastal and Marine Systems Science, Coastal Carolina University, Conway,

6   SC, 29526.

7   2) School of Zoology, Faculty of Life Sciences, Tel Aviv University, Tel Aviv 69978, Israel.

8   3) The Inter-University Institute for Marine Sciences, POB 469, Eilat 88103, Israel.

9   * Corresponding author: Roi Holzman <holzman@tauex.tau.ac.il>

10

11   Keywords: *Sparus aurata*, Reynolds numbers, feeding kinematics

12

13

14

15

16 **Abstract**

17 Fish larvae are the smallest self-sustaining vertebrates. As such, they face multiple challenge

18 that stem from their minute size, and from the hydrodynamic regime in which they dwell.

19 This regime of intermediate Reynolds numbers (*Re*) was shown to affect the swimming of

20 larval fish and impede their ability to capture prey. Numerical simulations indicate that the

21 flow fields external to the mouth in younger larvae result in shallower spatial gradients,

22 limiting the force exerted on the prey. However, observations on feeding larvae suggest that

23 failures in prey capture can also occur during prey transport, although the mechanism

24 causing these failures is unclear. We combine high-speed videography and numerical

25 simulations to investigate the hydrodynamic mechanisms that impede prey transport in

26 larval fishes. Detailed kinematics of the expanding mouth during prey capture by larval

27 *Sparus aurata* were used to parameterize age-specific numerical models of the flows inside

28 the mouth. These models reveal that, for small larvae that slowly expand their mouth, not

29 all the fluid that enters the mouth cavity is expelled through the gills, resulting in flow

30 reversal at the mouth orifice. This efflux at the mouth orifice was highest in the younger

31 ages, but was also high (>8%) in slow strikes produced by larger fish. Our modeling explains

32 the observations of "in-and-out" events in larval fish, where prey enters the mouth but is

33 not swallowed. It further highlights the importance of prey transport as an integral part in

34 determining suction feeding success.

35

36

37

38	**Introduction**
39	Most marine fish reproduce by broadcasting small (~1 mm in diameter) eggs into the open
40	ocean, providing no parental care from the hatching larvae (Blaxter, 1988; Cowen, 2002;
41	Houde, 1987). Typically, larvae deplete their yolk sac after a couple of days (usually 3-7,
42	depending on temperature and environmental conditions) and resort to feed autonomously
43	to gain the necessary resources to complete their development (Blaxter, 1988; Cowen,
44	2002; Houde, 1987). Despite the staggering variation in body size and life history strategies,
45	the small eggs and larvae, and the lack of parental care, are nearly ubiquitous across marine
46	fish (Barneche et al., 2018). Consequently, fish larvae are the smallest self-sustaining
47	vertebrates. Almost all larval fishes feed in the pelagic realm using "suction feeding", a
48	characteristic behavior in which fish sequentially open their mouth, expand their buccal
49	cavity and open the opercula covers to generate a unidirectional flow of water that carries
50	their prey into the mouth (Day et al., 2015; Holzman et al., 2015).
51	In the wild, larval fish suffer dramatic mortality rates (Hjort, 1914; Houde, 1987). It is
52	estimated that >90% of the brood is eradicated during the "critical period", extending from
53	the time of first feeding until the larvae is ready to settle in its juvenile habitat. During this
54	period, larval fish undergo dramatic morphological and developmental changes, including
55	the ossification of the cranium and vertebrae, the degradation of the fin fold and
56	development of fin rays, as well as the continuous growth and development of the eyes
57	(Blaxter, 1988; Kavanagh and Alford, 2003). Concomitantly, coordination and motor pattern
58	change and improve (Westphal and O'Malley, 2013). The physical growth of the larvae,
59	coupled with the development of stronger muscles that support faster movements lead to
60	an ontogenetic transition in the ways larvae interact with their fluid environment (China and
61	Holzman, 2014; Holzman et al., 2015). Being small and slow, young larvae live in a domain of

62   intermediate Reynolds numbers (*Re*), in which viscous forces are non-negligible compared

63   to inertial ones. This hydrodynamic regime was shown to impede the feeding rates of larval

64   fishes, with 8 Days Post Hatch (DPH) *Sparus Aurata* larvae failing to capture non-evasive

65   prey in ~80% of their feeding strikes (China and Holzman, 2014). Manipulations of the

66   viscosity of the medium in which larvae fed demonstrated that the feeding rates of larvae

67   were determined primarily by the hydrodynamic environment, described by the Reynolds

68   numbers that characterized the feeding events (China and Holzman, 2014; Holzman et al.,

69   2015). Older larvae (13 and 23DPH) that fed in a viscous medium displayed feeding rates

70   equivalent to those of the 8DPH larvae in unmanipulated water. Larvae that were raised in

71   mediums with increased viscosity expressed elevated levels of hunger-related

72   neuropeptides (Koch et al., 2018) and suffered higher mortality rates (Yavno and Holzman,

73   2018). Furthermore, the probability of executing successful prey-acquisition strikes

74   increased with increasing *Re* number calculated for the suction feeding strike (China et al.,

75   2017). Transition into higher Re also improves the larvae's ability to capture highly evasive

76   prey such as copepods (Jackson and Lenz, 2016; Sommerfeld and Holzman, 2019; Yaniv et

77   al., 2014).

78   Observations using high-speed videos indicate that one of the reasons for failure in

79   prey acquisition strikes is the occurrence of "in-and-out" events, in which prey is carried into

80   the mouth by the suction flows, but is expelled before the mouth is closed (China et al.,

81   2017; Holzman et al., 2015). The suction flows in these "in-and-out" events were

82   characterized by lower *Re* compared to those in successful events. Furthermore "in-and-

83   out" strikes were initiated from a further distance and were slower compared to

84   unsuccessful events in which the prey did not even enter the mouth (China et al., 2017). A

85   flow visualization study reported flow reversals in larval zebrafish, that occurred in smaller

86   larvae at the time when the mouth started closing (Pekkan et al., 2016). This is in sharp

87   contrast to adult fish, in which flow reversals are rare and minor (Jacobs and Holzman,

88   2018). However, the extent of these flow reversals across species and developmental stages

89   are unclear, as well as the hydrodynamic conditions under which they occur.

90   Here, we used computational fluid dynamics (CFD) to investigate the fluid dynamics

91   of suction feeding larval fish. Following Yaniv et al (Yaniv et al., 2014), we constructed a

92   model of an expanding buccal cavity, which incorporates an anterior-to-posterior wave of

93   buccal expansion (Bishop et al., 2008) over time. Our modeling included the opening of the

94   opercula covers at the posterior end of the mouth, a hallmark feature of suction feeding in

95   fishes, which generate unidirectional flows into the mouth while it is closing (Van

96   Wassenbergh, 2015). The model was parametrized based on observed strike kinematics of

97   *Sparus aurata* larvae ranging from first feeding to metamorphosis. Using these kinematics,

98   we quantified the flow speeds and the influx and efflux into the mouth and out of the gills

99   for six larval ages. We then characterized the extent of flow reversals, the flow conditions in

100   which they occur, and the role of hydrodynamics and kinematics (behavior) in driving these

101   flow reversals.

102

103   **Methods**

104   *Study organisms*

105   We reanalyzed high-speed videos of suction feeding gilthead sea-bream larvae

106   (*Sparus aurata* Linnaeus, 1758) feeding on Rotifers (*Brachionus rotundiformis*; ~0.16 mm in

107   length), from dataset previously used in China and Holzman, 2014 and China et al., 2017. *S.*

108   *aurata* is a pelagic spawner, hatching at ~3.5 mm. Feeding initiates at ~5 days post hatching

109   (DPH) at a body length of ~4 mm. Larvae reach the stage of flexion at ~21-24 DPH, at a

110   length of 7-10 mm, depending on conditions. *Brachionus rotundiformis* is a species of

111   planktonic rotifer, actively swimming at ~0.2 mm s^{-1}. Prey swimming speed is an order of

112   magnitude slower than the swimming speed of the larvae, and their escape response is

113   considered weak (China and Holzman, 2014; China et al., 2017). Rotifers are universally used

114   as the standard first-feeding food in the mariculture industry.

115   *High-speed videos*

116   Suction feeding events of larval fish were recorded using high speed video (500 and

117   1000 frames per second) as described in (China and Holzman, 2014; China et al., 2017). In

118   these experiments, fish swam freely in an aquarium, and their orientation with respect to

119   the camera included lateral, dorsal and ventral views. From the larger dataset of prey

120   acquisition strikes we selected 63 clips in which we could clearly track the kinematics of

121   mouth opening as well as either the hyoid (using lateral view of the fish) or the opercula

122   (using dorsal or ventral views) throughout prey acquisition strike. Clips were selected for

123   fish at the ages of 8, 12-13, 17-18, 22-25, 30 and 35-37 DPH (hereafter 8, 13, 18, 23, 30 and

124   37 DPH; 4-14 clips per age group). From the lateral view videos, we measured the time of

125   mouth opening and closing, maximal mouth diameter, the time of initiation and peak hyoid

126   displacement and its maximal excursion, and the time of opercula opening and closing

127   (when clearly visible). From the dorsal and the ventral view videos, we measured the time of

128   the mouth opening and closing, the time of initiation and peak opercula displacement and

129   its maximal excursion, and the corresponding parameters at the base of the opercula (1st gill

130   arch). To enable comparisons between different ages and strikes, we standardized the times

131   of hyoid and opercula excursions by the time to peak gape opening (TTPG) in each clip, and

132   their excursions by peak gape. Not all the parameters were visible in all the clips, resulting in

133   a sparse matrix that was ~60% full. We averaged the timing and excursion parameters for

134   each landmark, regressed them against larval age and used the predicted values from the

135   regression to generate characteristic kinematics for each age (table 1).

136   *Geometry of the modeled buccal cavity*

137   We build on a previous model of mouth cavity expansion suggested by (Bishop et al.,

138   2008; Yaniv et al., 2014), but added the opening of the opercular slits, a hallmark of suction

139   feeding across fishes (Van Wassenbergh, 2015).In brief, the model was composed of three

140   compartments of constant axial lengths, L_1, L_2 and L_3 (Fig. 1). These compartments

141   represented the region from the mouth opening to the anterior hyoid (L_1), the region

142   spanning the anterior to posterior length of the hyoid (L_2) and the region posterior to the

143   hyoid extending to the opening of the esophagus (L_3). Mouth cavity expansion was

144   simulated as time-dependent changes in the radii (, R_1, R_2, R_3, and R_4) of the bases of the

145   compartments, parametrized according to the observed kinematics of the corresponding

146   landmarks in our larvae (see above). The radius R_1 represents the radius of the gape. The

147   lengths B_1, B_2 and B_3 of the lateral surfaces of each compartment varied with time to fit the

148   length variations of the radii R_1, R_2 and R_3. We simulated mouth expansion for six larval ages

149   (8, 13, 18, 23, 30 and 37 DPH) with increasing gape diameter and mouth lengths. Internal

150   dimensions of L_1, L_2 and L_3 were 25%, 30% and 45% of the total mouth cavity length L, and

151   mouth radii before mouth expansion were set to 2.5% for R_1 and R_4, and 5% for R_2-R_3 (Yaniv

152   et al., 2014).

153   The pattern of mouth opening was simulated by varying the radii *R(t)* of each mouth

154   section (R_1-R_4) using the following time-dependent exponential function (Eq. 1; modified

155   from (Müller et al., 1982)):

156    $$R(t) = R_0 + (R_{max} - R_0) \left[\frac{t-t_0}{(t_{max}-t_0)} exp \left(1 - \frac{t_0-t}{(t_{max}-t_0)} \right) \right]^2 \qquad \text{(Eq. 1)}$$

157   Here, $R_0 = R(t=0)$, t_0 is the time when R first deviates from R_0 and t_{max} is the time

158 when R is maximal ($R=R_{max}$). Note that the radius of each mouth section can have different

159 R_0, t_0, R_{max} and t_{max} values (Table 1; Fig 3).

160   Feeding events used to parametrized our model were acquired using manually

161 triggered high-speed cameras, a method which might be biased towards capturing more

162 noticeable events i.e. faster or greater in excursion(China et al., 2017). Thus, they might

163 have represented higher- performance strikes. To investigate the effect of low-effort strikes

164 on the flow dynamics, we run our numerical simulations (see below) for the 23, 30, and 37

165 DPH cases using the observed geometry but with the expansion kinematics and the relative

166 timing of the 8 DPH case (time to peak gape of 57.3 ms, and time to peak R_2- R_4 of 70.3, 73.1

167 and 78.8 ms, respectively for all three models; Table 1).

168   *Computational approach*

169   To simulate the fluid dynamics of the buccal cavity and characterize the flow moving

170 in and out of the mouth cavity, a simplified model of an axi-symmetrical mouth cavity was

171 designed. The boundaries of the mouth cavity in the simulations presents a simplified

172 structure that has a cylindrical wall surrounding the cavity and unclosed inlet and outlet

173 edges at the right and left ends, respectively. The cylindrical wall sections are comprised of

174 three length sections that are flexibly connected, and their individual movement was

175 prescribed by the measured kinematics as explained in the kinematics section. To represent

176 the body of the fish and supplement the function of the gills, a streamlined elongated body

177 with a length similar to mouth length was designed downstream the buccal cavity. The body

178 had a small protruding part inside the cavity outlet, with a small (~10^{-3} mm) gap from the

179 buccal walls at $t = 0$. At $t > 0$ the mouth started expanding, drawing the fluid in through the

180   gape, followed by the opening of the gap (the gills) based on the prescribed kinematics for

181   R_4.

182   The mouth cavity was immersed in a fluid-filled rectangular domain, and it was

183   placed at the center of the domain. The rectangular fluid domain has six boundaries: inlet at

184   the right end, outlet at the left end and four walls (at the top, bottom, far and near) such

185   that uniform flow was formed to move in the domain from right to left. Water at standard

186   atmospheric condition was used as fluid material in the domain. A velocity inlet boundary

187   condition was used at the inlet with water flowing at 13 mm s^{-1} and pressure-outlet

188   boundary condition with standard atmospheric pressure was set at the domain outlet. The

189   top, bottom, far and near walls of the fluid domain, as well as the walls of the mouth cavity

190   were represented with no-slip boundary condition. As the inlet and outlet of the mouth

191   cavity were left unclosed, it is expected for the fluid to flow in and out of the mouth cavity

192   naturally depending on its kinematics. To ensure that the domain size does not interfere

193   with the flow inside and around the mouth cavity, the domain had sufficiently larger

194   dimensions: approximately 30 times the mouth cavity length along the X-direction (flow

195   direction) and 80 times the peak mouth opening radius along the Y-direction for each DPH

196   cases.

197   The flow field due to expansion of the mouth cavity model was governed by the

198   continuity and momentum conservation equations for incompressible viscous laminar fluid

199   flow in the absence of body force (Ferziger and Peric, 2001). General governing equations

200   for an unsteady, viscous laminar flow is given below.

$$\frac{\partial \rho}{\partial t} + \nabla . \rho \mathbf{V} = 0,$$

$$\frac{\partial \mathbf{V}}{\partial t} + \mathbf{V} . \nabla \mathbf{V} = -\frac{1}{\rho} \nabla p + \nu \nabla^2 \mathbf{V},$$

201   where ρ is fluid density, V is the velocity vector, p is the pressure and v is the kinematic

202   viscosity of the fluid. The flow governing equations were solved using finite volume based

203   commercial software package ANSYS fluent (ANSYS, Canonsburg, Pennsylvania). Mouth

204   cavity model was designed and meshed using ANSYS workbench (ANSYS, Canonsburg,

205   Pennsylvania). Unstructured (triangular shape) mesh method was chosen to discretize the

206   domain, the cavity and its boundaries. Relatively finer meshes were built inside and around

207   the mouth cavity while coarser meshes were used in the domain away from the cavity. To

208   simulate the expansion of the mouth cavity, dynamic mesh method was utilized. The

209   dynamic meshing corresponds to changing of the mesh geometry over time and space

210   based on the prescribed kinematics of the cavity. The kinematic motion of the mouth cavity

211   was prescribed within the fluent solver using the user defined function

212   'DEFINE_GRID_MOTION' (Ansys, 2009; Van Wassenbergh, 2015). This procedure was

213   performed using a user defined function that was compiled and assigned to each length

214   sections of the mouth cavity. Local cell re-meshing method was chosen to re-mesh the mesh

215   grids for every two timesteps based on minimum and maximum cell length and maximum

216   skewness parameters of each cell. To solve the flow equations, a SIMPLE scheme (Ansys,

217   2009) was employed to carry out the pressure-velocity calculations. Spatial discretization

218   was assigned with second order least square cell-based gradients method whilst a first order

219   implicit method was used for time discretization. The complete numerical solution was

220   obtained by ensuring that the convergence criteria of 10^{-4} for the continuity and the flow

221   speed components are attained. Before proceeding with the final simulations, mesh

222   convergence study was carried out to confirm stable solution is achieved and the mesh does

223   not influence the solution. For instance, for the 8 DPH case, we built three different meshes

224   with approximately, 90,000 cells, 140,000 cells and 300,000 cells. Mesh validation was

225   performed by comparing peak flow speed at both inlet and outlet for each mesh cases and

226   observed less than 1% variation between mesh 2 and 3. Then mesh with 140,000 cells was

227   chosen for the further simulation. Irrespectively for all the DPH cases the movement of

228   mouth cavity was simulated for 280 ms with 2,800 timesteps (each 10^{-4} s).

229   Flow speed at the inlet and outlet at each time step was calculated as the average of

230   flow speed across it. Correspondingly, peak flow speed was the flow speed at the time of

231   maximal mouth opening. Flow rates were defined as the product of flow speed and the

232   circular area of the inlet and outlet. Peak flow rate was flow rate at the time of maximal

233   mouth opening. Reynolds number (Re) was calculated as

$$Re = \frac{\upsilon L}{\nu}$$

234   where υ is flow speed (m s^{-1}), ν is the kinematic viscosity of the fluid (m^2 s^{-1}) and L is the

235   characteristic length scale (m). We used the swimming speed of the larvae as the

236   characteristic speed and the buccal length as the characteristic length.

237   Reynolds number was developed to characterize the flow in the case of steady flow

238   within a long rigid tube with a fixed (time independent) radius. However, the suction flow is

239   controlled by the rapid time-dependent motion of the cavity walls, and is characterized by

240   strong temporal flow patterns, which needs to be considered. We therefore propose to use

241   the Womersley number, α^2 which was formulated for pulsating flows mainly associated

242   with cardiovascular systems (Womersley, 1955), and is calculated as:

$$\alpha^2 = \frac{\omega L^2}{\nu}$$

243   where ω is the characteristic angular frequency (s^{-1}), ν is the kinematic viscosity of the fluid

244   (m^2 s^{-1}) and L is a characteristic length scale (gape; m). The Womersley number relates the

245   pulsation flow frequency to viscous effects. Here, the angular frequency is calculated using

246   the time it takes the larvae to fully open its mouth (TTPG) such that $\omega = 2\pi/TTPG$. Note

247   that we used different (although correlated) characteristic lengths for the Womersley and

248   Reynolds, referring to buccal length and gape, respectively.

249

250   **Results**

251   To facilitate the comparison between fish species in which the growth rates can differ, we

252   hereafter report on the scaling of suction feeding kinematics and dynamics with buccal

253   length. As larvae mature from 8 DPH to 37 DPH, the length of the buccal cavity and the

254   diameter of the mouth increase by about two-fold (Fig 2; Table 1). Concomitantly, the time

255   to peak gape decreases by a factor of ~3.6 from an average of 57.3 ms at 8 DPH to 15.6 at

256   37 DPH. By and large, the kinematics observed in *S. aurata* larvae yielded unidirectional

257   flows in our CFD models, i.e. fluid entering the mouth at the gape (inlet; Fig 5A) and exiting

258   through the gills (outlet; Fig 5B). As previously reported (Yaniv et al., 2014), peak flow

259   speeds at the mouth inlet (U_{peak}(gape)) increased with increasing buccal length (i.e. age; *L*),

260   following the exponential relationship U_{peak}(gape) = -0.56*exp(3.39 L); (Fig 6A). Peak flow

261   speed was 28.3 mm s^{-1} for the 8 DPH case and increased to 49.8 and 136.2 mm s^{-1} for the 23

262   and 37 DPH cases. Correspondingly, *Re* increases by an order of magnitude (from 23 at 8

263   DPH to 218 at 37 DPH).

264   Similarly, peak flow rate at the mouth inlet (Q_{peak}(gape)) increased with increasing

265   buccal length from 0.58 mm^{3} s^{-1} for the 8 DPH case to 2.96 and 8.37 mm^{3} s^{-1} for the 23 and

266   37 DPH cases, following an exponential relationship Q_{peak}(gape)= -0.021*exp(3.71 L) (Fig 6c).

267   Peak flow rate at the outlet Q_{peak}(gills) increased with increasing buccal length from 0.13

268   mm^{3} s^{-1} for the 8 DPH case to 0.93 and 2.26 mm^{3} s^{-1} for the 23 and 37 DPH cases, following

269   an exponential relationship Q_{peak}(gills)= -0.0056*exp(3.7 L).

270 While the observed kinematics in all cases (8-37 DPH) resulted in a net influx into the

271 gape (inlet), we observed considerable efflux (flow reversals) around the time of mouth

272 closure (Fig 5B). These flow reversals were most pronounced for models depicting suction

273 feeding in young (8 and 13 DPH) ages, where efflux out of the gape was ~10% and ~3% of

274 the influx into the cavity, respectively (Fig 6). Efflux decreased sharply for the cases of 18-37

275 DPH (Fig 6). Plotting the Reynolds *versus* Womersley numbers for all our cases (Fig 7)

276 indicated that efflux at the mouth (flow reversals) was > 3% of the influx for the smaller

277 larvae, characterized by Re < 50 and a^2 < 4. Furthermore, running the model for the 23, 30

278 and 37 DPH cases using the observed morphology excursions but the kinematics of the 8

279 DPH case yielded high efflux (~7-8%), similar to the ones obtained for the 8 DPH case (Fig 7).

280

281 **Discussion**

282 In this study, we used computational fluid dynamics (CFD) to investigate the fluid dynamics

283 of suction feeding larval fish. Using observed strike kinematics of *Sparus aurata* larvae

284 ranging from first feeding to metamorphosis to parametrize the model, we quantified the

285 flow speeds and the influx and efflux into the mouth and out of the gills for six larval ages.

286 As larvae grow, their buccal cavity elongated and its radii increase, and it expands faster (Fig

287 2, Table 1). These kinematics leads to an increase in the maximal flow speed and flow rate

288 observed at the orifice (Fig 5, 6). While most of the fluid entrained in the cavity is evacuated

289 through the gills, we observed high efflux of water flowing outwards from the gape (Fig 5,7).

290 These flows occurred predominantly in the models characterized by Re < 50 and a^2 < 4, but

291 also in our larger models during slow mouth opening. Overall, our results show that the

292 inability of larval fish to capture prey may result from (at least) two hydrodynamic

293 mechanisms: (1) their suction force do not exert sufficient force to draw the prey into the

294   mouth (Yaniv et al., 2014), and (2) flow reversals may carry the prey outside as the mouth

295   closes if the prey did not get deep enough into the mouth (this study; (China et al., 2017;

296   Holzman et al., 2015)).

297   Previous observations of larval feeding on non-evasive prey indicate the prevalence of

298   "in-and-out" events where prey that entered the mouth was expelled before the mouth

299   closed (China et al., 2017; Holzman et al., 2015). The probability of these "in-and-out"

300   events increased in suction feeding events characterized by low Re (<20), compared to

301   successful events characterized by higher Re of >40 (China et al., 2017). This observation is

302   in agreement with our results, indicating the prevalence of high efflux (flow reversals) under

303   low Re, a condition characterizing younger larvae or older larvae that execute low-effort

304   strikes. Furthermore, flow reversal in the models occurred later in the strike, as the mouth

305   was closing. This timing corresponds to the observation of the "in-and-out" events, and the

306   fact that they were initiated from a further distance compared to unsuccessful events in

307   which the prey did not enter the mouth at all (China et al., 2017). A flow visualization study

308   reported flow reversals in larval zebrafish, occurring in when the mouth starts closing

309   (Pekkan et al., 2016). However, that study did not report the hydrodynamic or kinematic

310   correlates were associated with their occurrence. For larger fish that operate at higher Re

311   (Re >55 for 75% of >400 PIV measurements; (Jacobs and Holzman, 2018)) such flow

312   reversals were extremely rare. In general, whether prey transport during suction feeding

313   can hinder feeding success is rarely demonstrated.

314   Reynolds number is commonly used to characterize the suction flow field for adults

315   and well as larval fishes (China and Holzman, 2014; China et al., 2017; Hernández, 2000;

316   Holzman et al., 2015). Reynolds number provides the ratio between inertia and viscous

317   forces; as Reynolds increase, inertia forces are considered dominated over viscous ones and

318   vice versa. Reynolds number is frequently used to determine if the flow is laminar or

319   turbulent (Denny and Wethey, 2001; Vogel, 1994) and for specific configurations, critical

320   Reynolds numbers were proposed. However, given the nature of the flow within the buccal

321   cavity, we suggest that Reynolds might not convey all the information needed to

322   characterize the fluid phenomena. Reynolds number was developed to characterize the flow

323   in the case of steady flow within a long rigid tube with a fixed (time independent) radius.

324   However, the suction flow is a pressure driven flow, controlled by the rapid time-dependent

325   motion of the cavity walls (Day et al., 2015). Hence, the boundary conditions change as the

326   cavity opens and close over a short period of time, indicating that suction feeding is not only

327   a pressure driven phenomena but also a transient one. Therefore, one should consider, in

328   addition to the inertia and viscous effects, the temporal ones. Furthermore, to characterize

329   a suction feeding event based on Re, one should choose a characteristic lengths and speed

330   out of several possible options: for example one could justify using peak gape, or gape at

331   the time of peak flow speed, or mean gape, and that choice would change the calculated Re.

332   We therefore proposed to use the Womersley number, α^2 which was formulated for

333   pulsating flows mainly associated with cardiovascular systems (Womersley, 1955). While it

334   is acknowledged that, for the case of suction feeding the repetition rate is low (i.e. unlike

335   cardiovascular systems, the time between consecutive suction events is relatively long), the

336   temporal parameter is dominant. Admittedly, Reynolds and Womersley numbers for

337   different cases can be correlated because in some instances the length scales (gape and

338   mouth length) are correlated, as well as the suction flow speed can be correlated with gape

339   size and TTPG (Jacobs and Holzman, 2018), however we advise that future studies of suction

340   feeding dynamics report the relevant Womersley number for their case. We re-analyzed

341   data from (China et al., 2017) and found that failed strikes were characterized by mean

342     $\alpha^2 = 1.01 \pm 0.5$, "in and out" events had $\alpha^2 = 1.31 \pm 0.46$ and successful strikes had

343     $\alpha^2 = 2.16 \pm 1.33$, supporting the usefulness of α^2 to understand larval feeding.

344   We suggest that the flow reversals stem from the boundary layer that develops near

345   the mouth's walls, slowing the flow through the mouth. To approximately calculate the

346   boundary layer thickness (δ_{BL}) inside the mouth cavity and to illustrate its trend as a

347   function of the mouth length and DPH, we utilized Blasius's boundary layer theory for low-

348   viscosity flow over a long plate (Falkneb and Skan, 1931). While several assumptions of the

349   Blasius's solution were not met in our case (e.g. steady flow over long flat plate with no

350   pressure gradients along the flow direction), this solution should reasonably predict the

351   trend in the thickness of the boundary layer. According to this solution, the boundary layer

352   thickness is approximated as:

$$\delta_{BL} = \frac{5.0}{\sqrt{Re_L}}$$

353   where Re_L, is the Reynolds number based on the length of semi-infinite plate. In our case,

354   we choose to estimate the boundary later thickness over the second axial length (L$_2$) of the

355   mouth cavity at an instant after the peak mouth opening where the L$_2$ is almost flat and

356   parallel to the downstream flow. We identified the time instant for the case of each DPH

357   such as 80.4 ms, 80.4 ms, 77.5 ms, 71.7 ms, 51.5 ms, and 34.4 ms for 8, 13, 18, 23, 30, and

358   37 DPH, respectively. At a given time, the flow velocity of the region inside the cavity over

359   the length, L$_2$ alone was averaged and this averaged flow velocity and the length, L$_2$ was

360   used to calculate the Reynolds number (Re_L). As expected, the thickness of the boundary

361   layer decreased with increasing age. The degree of efflux exponentially increased as a

362   function of the ratio between boundary layer thickness and gape diameter, suggesting that

363   the development of slower flows near the cavity walls and the mouth openings could be

364   responsible for the flow reversal.

365   Previous measurements (Pekkan et al., 2016), modeling (Yaniv et al., 2014) and

366   estimations based on buccal dynamics (China et al., 2017) reported peak suction flows

367   ranging ~1-40 mm s^{-1}, for range of buccal length parameters (i.e. gape diameter)

368   corresponding to the current study. While PIV measurements and CFD simulations of larval

369   fish represent a limited sample of individuals, high-speed videos suggest that the variation

370   in peak flow speed among individuals can be substantial (China et al., 2017). Similarly, PIV

371   studies on adult fish indicate broad variation in peak flow speed for repeated strikes by the

372   same individuals (Day et al., 2015; Holzman et al., 2008; Jacobs and Holzman, 2018). Such

373   variation was not included in our study. Moreover, we base our modeling based on feeding

374   events acquired using manually triggered high-speed cameras, and it is more likely that an

375   observer operating it will notice and trigger an event when it is faster and greater in

376   excursion. Thus, one should use the flow velocities estimated in our study as an example of

377   high, rather than average, larval performance.

378

379

380 **References**

381 **Ansys, F.** (2009). *12.0 Theory Guide*. 5.5. Ansys Inc.

382 **Barneche, D. R., Burgess, S. C. and Marshall, D. J.** (2018). Global environmental drivers of

383   marine fish egg size. *Glob. Ecol. Biogeogr.* **27**, 890–898.

384 **Bishop, K. L., Wainwright, P. C. and Holzman, R.** (2008). Anterior-to-posterior wave of

385   buccal expansion in suction feeding fishes is critical for optimizing fluid flow velocity

386   profile. *J. R. Soc. Interface* **5**, 1309–16.

387 **Blaxter, J. H. S.** (1988). 1 Pattern and Variety in Development. *Fish Physiol.* **11**, 1–58.

388 **China, V. and Holzman, R.** (2014). Hydrodynamic starvation in first-feeding larval fishes.

389   *Proc. Natl. Acad. Sci. U. S. A.* **111**, 8083–8.

390 **China, V., Levy, L., Liberzon, A., Elmaliach, T. and Holzman, R.** (2017). Hydrodynamic

391   regime determines the feeding success of larval fish through the modulation of strike

392   kinematics. *Proc. R. Soc. B Biol. Sci.* **284**,.

393 **Cowen, R. K.** (2002). Chapter 7 - Larval Dispersal and Retention and Consequences for

394   Population Connectivity. In *Coral Reef Fishes. Dynamics and Diversity in a Complex*

395   *Ecosystem* (ed. Sale, P. F.), pp. 149–170. San Diego: Academic press.

396 **Day, S. W., Higham, T. E., Holzman, R. and Van Wassenbergh, S.** (2015). Morphology,

397   Kinematics, and Dynamics: The Mechanics of Suction Feeding in Fishes. *Integr. Comp.*

398   *Biol.* **55**, 21–35.

399 **Denny, M. and Wethey, D.** (2001). Physical processes that generate patterns in marine

400   communities. In *Marine Community Ecology* (ed. Bertness, M. D.), Gaines, S. D.), and

401   Hay, M. E.), pp. 3–37. Sunderland, MA (USA): Sinauer Associates.

402 **Falkneb, V. M. and Skan, S. W.** (1931). LXXXV. *Solutions of the boundary-layer equations.*

403   *London, Edinburgh, Dublin Philos. Mag. J. Sci.* **12**, 865–896.

404 **Ferziger, J. H. and Peric, M.** (2001). *Computational methods for fluid dynamics*. Springer.

405 **Hernández, L. P.** (2000). Intraspecific scaling of feeding mechanics in an ontogenetic series

406 of zebrafish, Danio rerio. *J. Exp. Biol.* **203**, 3033–43.

407 **Hjort, J.** (1914). Fluctuations in the great fisheries of northern Europe. Rapp. Pa-V. *Reun.*

408 *Cons. Perm. Int. Explor. Mer* **19**, 1–228.

409 **Holzman, R., Collar, D. C., Day, S. W., Bishop, K. L. and Wainwright, P. C.** (2008). Scaling of

410 suction-induced flows in bluegill: morphological and kinematic predictors for the

411 ontogeny of feeding performance. *J. Exp. Biol.* **211**, 2658–68.

412 **Holzman, R., China, V., Yaniv, S. and Zilka, M.** (2015). Hydrodynamic Constraints of Suction

413 Feeding in Low Reynolds Numbers, and the Critical Period of Larval Fishes. *Integr.*

414 *Comp. Biol.* **55**, 48–61.

415 **Houde, E. D.** (1987). Fish Early Life Dynamics and Recruitment Variability. In *American*

416 *Fisheries Society Symposium*, pp. 2: 17-29.

417 **Jackson, J. M. and Lenz, P. H.** (2016). Predator-prey interactions in the plankton: larval fish

418 feeding on evasive copepods. *Sci. Rep.* **6**, 33585.

419 **Jacobs, C. and Holzman, R.** (2018). Conserved spatio-temporal patterns of suction-feeding

420 flows across aquatic vertebrates: a comparative flow visualization study. *J. Exp. Biol.*

421 **221**, 1:11.

422 **Kavanagh, K. D. and Alford, R. A.** (2003). Sensory and skeletal development and growth in

423 relation to the duration of the embryonoic and larval stages in damselfishes

424 (Pomacentridae). *Biol. J. Linn. Soc.* **80**, 187–206.

425 **Koch, L., Shainer, I., Gurevich, T. and Holzman, R.** (2018). The Expression of agrp1 , A

426 Hypothalamic Appetite-Stimulating Neuropeptide, Reveals Hydrodynamic-Induced

427 Starvation in a Larval Fish. *Integr. Org. Biol.* **1**,.

428   **Pekkan, K., Chang, B., Uslu, F., Mani, K., Chen, C. Y. and Holzman, R.** (2016).

429   Characterization of zebrafish larvae suction feeding flow using???PIV and optical

430   coherence tomography. *Exp. Fluids* **57**,.

431   **Sommerfeld, N. and Holzman, R.** (2019). The interaction between suction feeding

432   performance and prey escape response determines feeding success in larval fish. *J. Exp.*

433   *Biol.* **222**, jeb204834.

434   **Van Wassenbergh, S.** (2015). A Solution Strategy to Include the Opening of the Opercular

435   Slits in Moving-Mesh CFD Models of Suction Feeding. *Integr. Comp. Biol.* **55**, 62–73.

436   **Vogel, S.** (1994). *Life in moving fluids: the physical biology of flow. Second edition.* Princeton

437   University Press.

438   **Westphal, R. E. and O'Malley, D. M.** (2013). Fusion of locomotor maneuvers, and improving

439   sensory capabilities, give rise to the flexible homing strikes of juvenile zebrafish. *Front*

440   *Neural Circuits* **7**, 108.

441   **Womersley, J. R.** (1955). Method for the calculation of velocity, rate of flow and viscous

442   drag in arteries when the pressure gradient is known. *J. Physiol.* **127**, 553–563.

443   **Yaniv, S., Elad, D. and Holzman, R.** (2014). Suction feeding across fish life stages: flow

444   dynamics from larvae to adults and implications for prey capture. *J. Exp. Biol.* **217**,

445   3748–57.

446   **Yavno, S. and Holzman, R.** (2018). Do viscous forces affect survival of marine fish larvae?

447   Revisiting the 'safe harbour' hypothesis. *Rev. Fish Biol. Fish.* **28**, 201–212.

448

449   Table 1: kinematics characteristics of larval fish used to parametrize the numerical model

| Age (DPH)	Buccal cavity length (mm)	Maximal gape diameter (mm)	Swimming speed (mm/s)	Time to peak gape (s)	Re_L	inlet		outlet		$\dfrac{Efflux}{influx}$ at inlet (%)
						Peak flow speed (mm/s)	Peak flow rate (mm³/s)	Peak flow speed (mm/s)	Peak flow rate (mm³/s)	
Observed kinematics										
8	0.81	0.11	8.1	57.3	22.8	28.3	0.58	8.50	0.13	10.1
13	1.06	0.15	10.6	50.1	24.4	23.1	1.37	11.1	0.35	3.1
18	1.23	0.17	12.3	42.9	44.1	35.9	2.24	14.3	0.61	1.3
23	1.36	0.19	13.6	35.7	67.6	49.8	2.96	17.3	0.93	0.34
30	1.50	0.21	15.0	25.7	121.3	81.3	5.22	17.4	1.12	0.26
37	1.61	0.23	16.1	15.6	218.2	136.2	8.36	30.9	2.26	0.06
Low effort strikes										
23	1.36	0.19	13.6	57.3	55.2	40.7	2.6	12.6	0.62	8.2
30	1.50	0.21	15.0	57.3	72	48.2	3.8	13.6	0.73	8.0
37	1.61	0.23	16.1	57.3	81.2	50.7	4.7	15.2	1.01	7.4

450
451
452

453   Fig. 1: A schematic description of the model geometry. Solid black bars indicate the location

454   of the buccal walls under maximal expansion, light shaded ones show the buccal walls at

455   rest (minimal volume). The mouth is modeled as three attached cones that expend

456   sequentially. L1-L3 correspond to the length of the three cones, whereas R1-R4 is the time-

457   dependent radii of the cones. R1 is the gape (inlet). An increase in R4 represents the

458   opening of the gill slits.

459

460
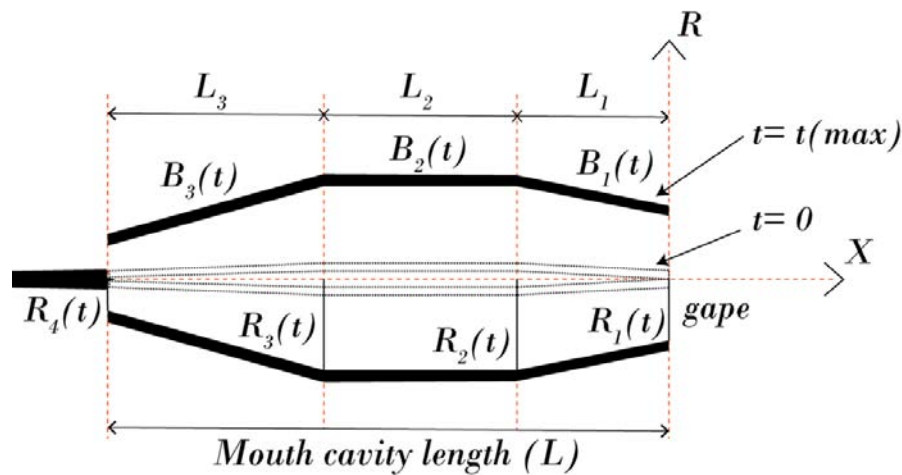
461

462

463

464

465   Fig 2. The relationships between age and gape diameter (A) and between gape diameter

466   and buccal length (B) in *Sparus aurata* larvae ranging 8-37 DPH (n=22 individuals). Blue lines

467   depict a linear regression between the two parameters (R^2 = 0.55 and 0.65 for A and B

468   respectively, P< 0.001 for both).

469
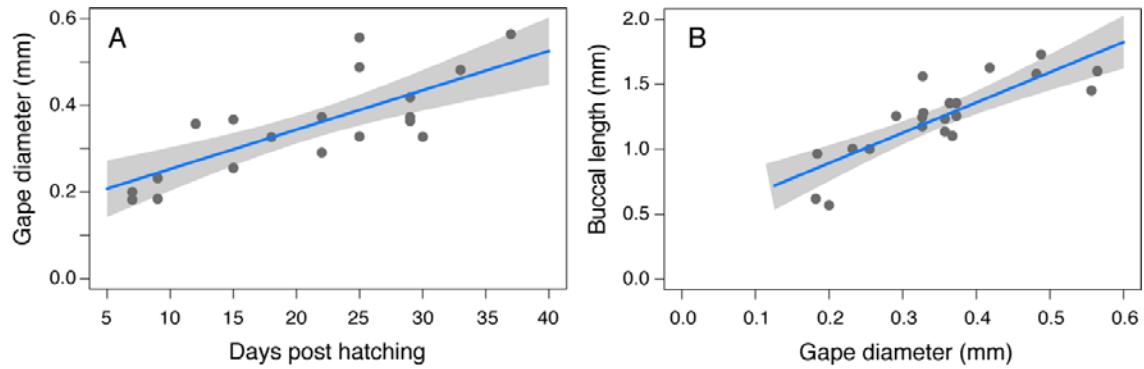
470

471

472

473

474 Fig 3. Buccal expansion kinematics across *S. aurata* ontogeny. Plots depict the radii of R_1-R_4

475 as a function of time for 8, 13, 18, 23, 30 and 37 DPH larvae. Note that as larvae grow the

476 overall time from mouth opening (R_1) to the closing of the gills (R_4) decreases, whereas the

477 radii (and correspondingly buccal volume) increase. Furthermore, the timing of peak radius

478 for each one of the mouth sections R_1-R_4 changes through larval growth.

479
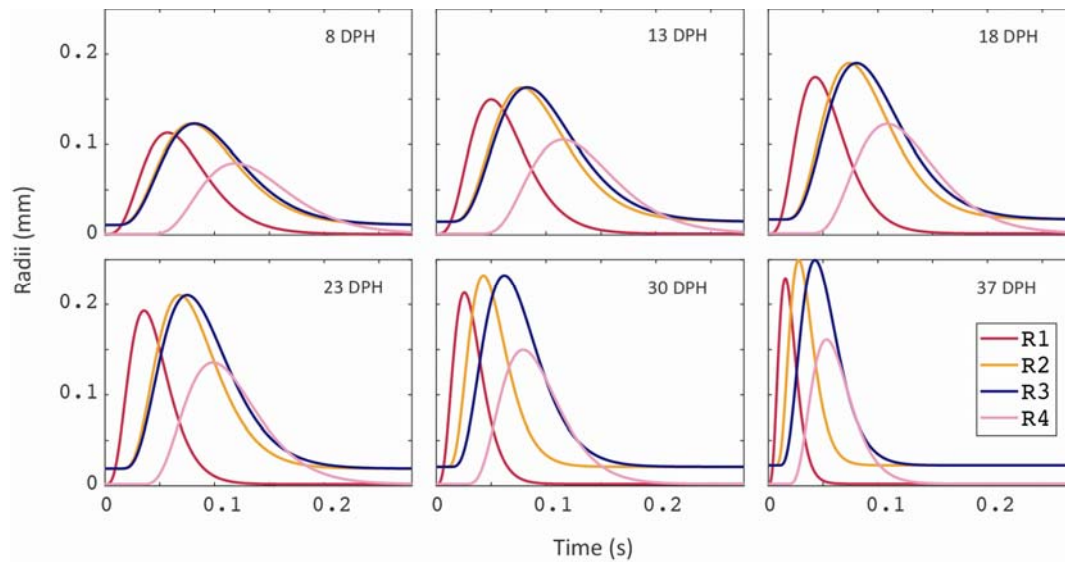
480

481

482   Fig 4: vector maps showing peak flow reversal for CFD models of 8, 13, 23, and 30 DPH

483   larvae. Vector maps for each age were saved at the time when efflux (flux into the orifice)

484   was maximal . Different x, y and speed scale are used in the four panels, however green

485   color consistently represents low (and zero) flows. Also note that gape size at peak efflux

486   decreases with increasing age.

487
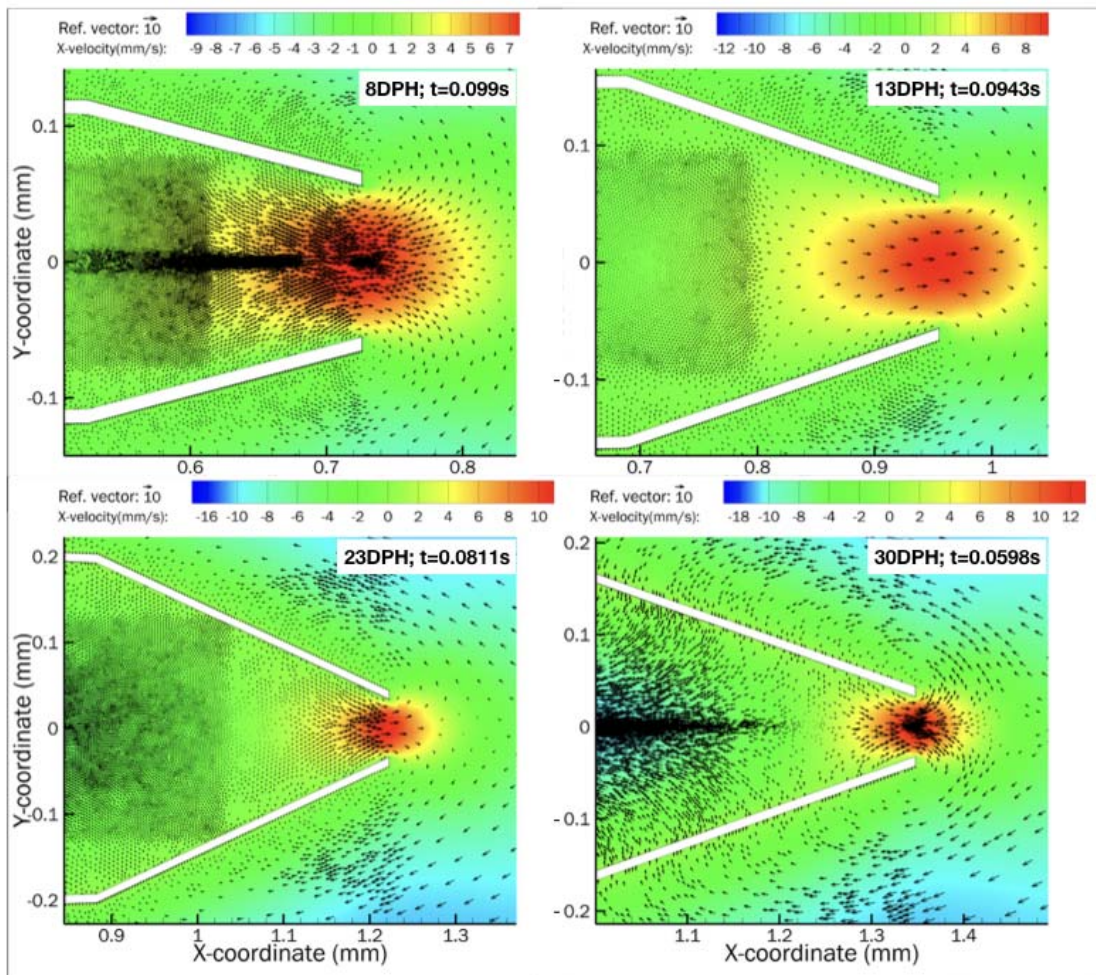
488
489

490   Fig. 5: Gape size and flow rates as a function of time. Drawn are (A) the radius of R_1 (gape

491   size), (B) the influx into the mouth inlet (gape), (C) the efflux out of the gills and (D) the

492   efflux out of the mouth inlet. As larvae grow, the influx at the gape and efflux at the gill

493   increase, however the efflux at the gape (flow reversals; positive flow rate) decreases. Note

494   the different scales and units for the Y-axes in A-D.
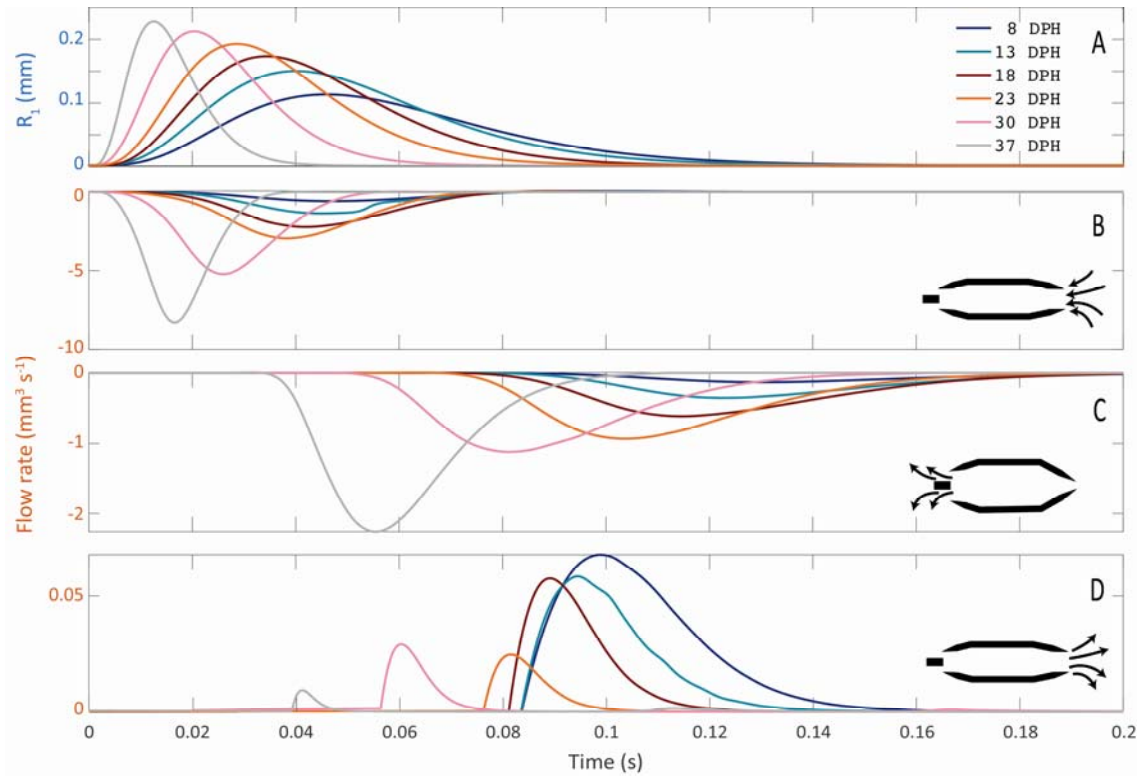
495

496

497   Fig 6: Scaling of peak flow speeds (A, B) and flow rates (C, D). Left column (A, C) depicts the

498   inlet, right column (B, D) depicts outlet. Black lines represent exponential fits. Colors depict
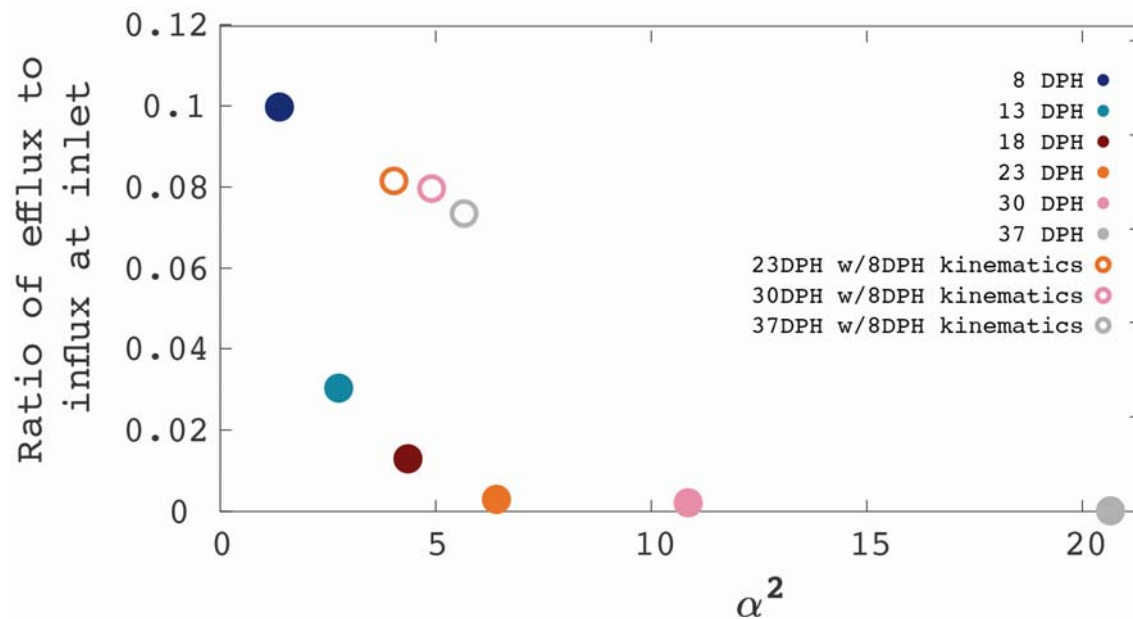
499   the different ages.
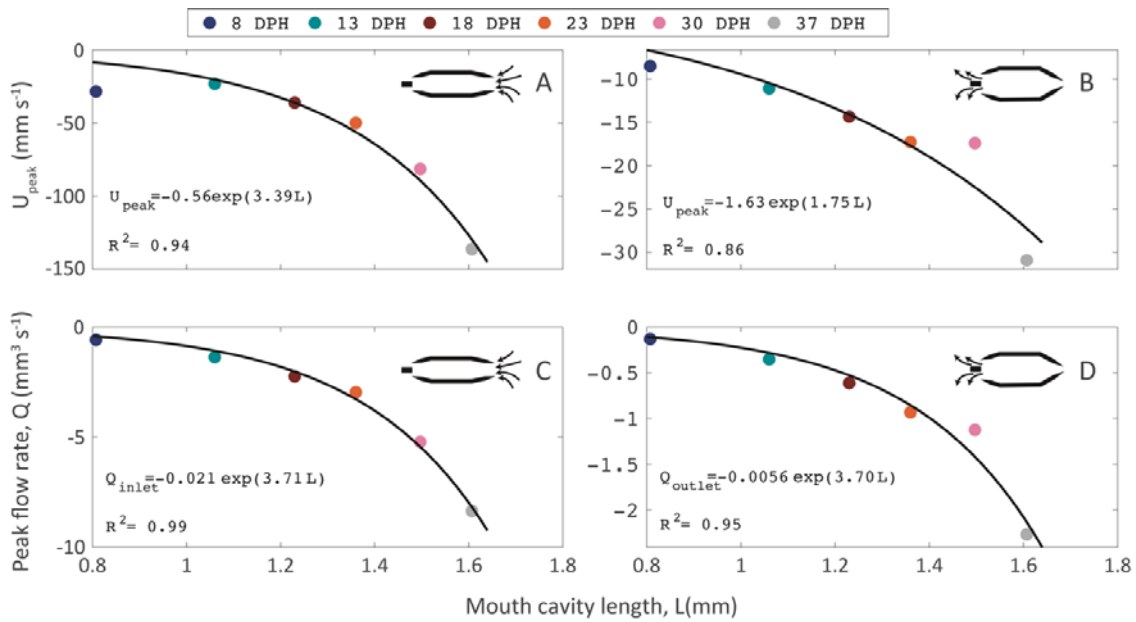
500

501

502

503   Fig 7: Hydrodynamic characterization of flow reversals. (A) the ratio of efflux to influx at the

504   inlet (gape) decays as Womersley number decrease, and is most prominent at $a^2 < 4$,

505   indicating that flow reversals occur under conditions where viscous effects dominate over

506   temporal (wall movements) effects. Full symbols represent the observed kinematics; open

507   symbols represent larger models where peak excursion and time to peak excursions were

508   similar to the 8DPH case, representing "low-effort" strikes.

509

510

511

512

513

514